Hydrothermal Synthesis | *Hot Paper*

# A Fast, Low-Temperature Synthesis Method for Hexagonal $YMnO_3$: Kinetics, Purity, Size and Shape as Studied by In Situ X-ray Diffraction

Kenneth P. Marshall,[a] Anders B. Blichfeld,[a] Susanne L. Skjærvø,[a] Ola G. Grendal,[a] Wouter van Beek,[b] Sverre M. Selbach,[a] Tor Grande,[a] and Mari-Ann Einarsrud*[a]

**Abstract:** The reaction mechanisms, phase development and kinetics of the hydrothermal synthesis of hexagonal-$YMnO_3$ from $Y_2O_3$ and $Mn_2O_3$ using in situ X-ray diffraction are reported under different reaction conditions with temperatures ranging from 300 to 350 °C, and using 1, 5 and 10 M KOH, and 5 M NaOH mineraliser. Reactions initiated with $Y_2O_3$ hydrating to $Y(OH)_3$, which then dehydrated to YO(OH). Higher temperatures and KOH concentrations led to faster, more complete dehydrations. However, 1 M KOH led to YO(OH) forming concurrently with $Y(OH)_3$ before $Y(OH)_3$ fully dehydrated but yielded a very low phase purity of hexagonal-$YMnO_3$. Using NaOH mineraliser, no YO(OH) was observed. Dehydration also initiated at a higher temperature in the absence of $Mn_2O_3$. The evolution of Rietveld refined scale factors was used to determine kinetic information and approximate activation energies for the reaction. The described hydrothermal synthesis offers a fast, low-temperature method for producing anisometric h-$YMnO_3$ particles.

## Introduction

Hexagonal $YMnO_3$ (h-$YMnO_3$) is a multiferroic material with simultaneous ferroelectric and antiferromagnetic properties.[1–7] These properties have led to a large research interest due to the possibility for ferroelectric-antiferromagnetic coupling,[8] allowing for potential applications in, for example, antiferromagnetic memory devices.[9] In addition to their ferroic properties, hexagonal manganites also display oxygen storage capacity,[10] which may be useful as oxygen membranes in gas separation or hydrogen fuel cell applications. h-$YMnO_3$ has also been reported to display photocatalytic properties,[11] and for this application, small particles with high surface area are most appropriate.

h-$YMnO_3$ crystallises in the space group $P6_3cm$ at room temperature.[12] There exists an orthorhombic perovskite phase of $YMnO_3$ (o-$YMnO_3$) which is kinetically stable at room temperature, and is the thermodynamically stable phase at high pressure due to its higher density compared with h-$YMnO_3$.[13,14] At room temperature, the most stable phase in the Y-Mn-O system is $YMn_2O_5$, as determined by Chen et al.,[15] who calculated the phase diagram for this system at atmospheric pressure in air. According to this work, h-$YMnO_3$ becomes the most thermodynamically stable phase above 789 °C.

Solid-state and sol-gel methods are well established to prepare highly pure h-$YMnO_3$. Both methods have the drawback of requiring at least one high temperature crystallisation step above 789 °C, where h-$YMnO_3$ becomes the most thermodynamically stable phase. The sol-gel method has been used to prepare nanoparticles with control over the crystal and grain size based on the crystallisation temperatures in the range of 800–1100 °C, giving particle sizes of the order of 100 nm. However, in addition to the high temperature required, another drawback is the amount of time and number of steps required; amorphous precursors require drying from solution at around 150 °C, calcination at ≈500 °C, and crystallization to form h-$YMnO_3$.[12,16,17] Additionally, our previous studies on the sol-gel synthesis of h-$YMnO_3$ have highlighted the effect of oxidising and reducing conditions on the outcome of the reaction; oxidising conditions were shown to lead to a higher amount of orthorhombic phase, due to the smaller $Mn^{IV}$ B-site cation causing the perovskite structure to become more geometrically favourable.[10,16,18]

Hydrothermal synthesis, in contrast to other methods, typically requires only one step, is performed at lower tempera-

[a] Dr. K. P. Marshall, Dr. A. B. Blichfeld, Dr. S. L. Skjærvø, Dr. O. G. Grendal, Prof. S. M. Selbach, Prof. T. Grande, Prof. M.-A. Einarsrud
Department of Materials Science and Engineering
NTNU—Norwegian University of Science and Technology
Sem Sælands vei 12, 7034 Trondheim (Norway)
E-mail: mari-ann.einarsrud@ntnu.no

[b] Dr. W. van Beek
Swiss-Norwegian Beamlines
European Synchrotron Radiation Facility
71 avenue des Martyrs, CS 40220, 38043 Grenoble Cedex 9 (France)

Supporting information and the ORCID identification number(s) for the author(s) of this article can be found under: https://doi.org/10.1002/chem.202000528.



Part of a Special Issue on Low Temperature Solution Route Approaches to Oxide Functional Nanoscale Materials.

tures, and can give phase pure products from reactions lasting only a matter of hours. Still, challenges remain in synthesising h-$YMnO_3$ hydrothermally, especially the range of oxidation states that Mn is capable of adopting, since Mn is stable from +2 to +4, with +2 being the most stable state.[19] Manganese is not stable in the +3 oxidation state in water, therefore the possibility for $Mn^{3+}$ to disproportionate in solution adds a considerable challenge for the hydrothermal synthesis of $YMnO_3$. Indeed, experimental evidence and theoretical calculations have shown that h-$YMnO_3$ is capable of accommodating significant oxygen interstitial defects, compensated by the presence of $Mn^{IV}$, up to an oxygen stoichiometry of $YMnO_{3.14}$.[20,21] This variable oxidation state gives rise to a stable secondary phase in the system, $YMn_2O_5$. o-$YMnO_3$ can also form as it has a Goldschmidt tolerance factor ($t$) of 0.80 and an octahedral factor ($\mu$) of 0.51 (high spin), which is within the range in which oxide perovskites can form ($\mu > 0.425$, and $0.906–0.232\mu < t < 1$).[22,23] In literature, there have been two reported pathways for synthesising h-$YMnO_3$ by hydrothermal routes. One method was reported by Stampler et al.[24] in which hexagonal $LnMnO_3$ (Ln = Ho–Lu, or Y) was synthesised from the oxides with KOH mineraliser (although results for Ln = Y were not included in the manuscript). The use of a high-temperature autoclave was required for the larger rare earth metals due to the higher stability of $Ln(OH)_3$. In an alternative method, aqueous $Y(NO_3)_3$, a $Mn^{II}$ salt, and $KMnO_4$ were reacted with KOH,[25] or NaOH,[26] at 240 °C. This latter route has been used to obtain particles with hexagonal[25] and nanorod[26] shapes. Under similar conditions to this route, Zhou et al. synthesised o-$YMnO_3$.[27] The primary difference between the two routes appears to be that a lower concentration of KOH and a lower filling factor are required to form the hexagonal phase compared with the orthorhombic phase.

The work by Stampler et al.[24] on the hydrothermal synthesis of hexagonal manganites highlighted the importance of temperature with regards to the choice of Ln atom, inferring that the $Ln_2O_3$ is converted to $Ln(OH)_3$ which then dehydrates to LnO(OH). However, the reaction progression at different temperatures and what happens with the $Mn_2O_3$ during the reaction remain uncertain.

In situ X-ray diffraction (XRD) during hydrothermal synthesis is a technique that has been used since the 1990s, with early papers having been published on zeolites by Norby et al.[28,29] Walton and O'Hare published an early review on the topic (for both hydrothermal and solid-state reactions) in 2000.[30] In situ neutron diffraction,[31] energy dispersive XRD,[32] and angle dispersive XRD[28] have all been used to monitor the process of crystallisation by hydrothermal synthesis. In situ diffraction has been used to probe, among other systems, the formation under hydrothermal conditions of functional binary metal oxide nanoparticles,[33–35] and several ferroic materials, including $BaTiO_3$,[36–38] $K_{1-x}Na_xNbO_3$,[39,40] $BiFeO_3$,[41] and $Sr_{1-x}Ba_xNbO_3$.[42]

Here we report in situ hydrothermal synthesis of h-$YMnO_3$ from $Y_2O_3$ and $Mn_2O_3$ at temperatures in the range of 300 to 350 °C monitored by synchrotron XRD. This study has allowed us to quantitatively measure the phases which appear over the course of the reaction, thereby revealing the reaction progression and kinetics, under different conditions. We have also studied the effect of hydrothermal conditions on $Y_2O_3$ to reveal the formation of the different hydroxides under increasing temperature. The results are discussed in relation to those obtained using ex situ techniques from reactions performed in a high-temperature autoclave.

## Results and Discussion

### In situ XRD-determined reaction progressions

Figures 1 (a)–(d) show the weight fractions of observed phases over time for in situ reactions between $Y_2O_3$ and $Mn_2O_3$ in 5 M KOH at 300, 320 and 350 °C, and in 5 M NaOH at 320 °C monitored by synchrotron XRD. Integrated XRD patterns and patterns calculated using Rietveld refinement of the final dataset of the reactions are included in Figures 1 (e)–(g). The 2D plot of the XRD patterns over time, along with the refined patterns at the beginning, intermediate period and end of the reaction at 320 °C in 5 M KOH are shown in Figures S1 (a) and (b) in Sup-

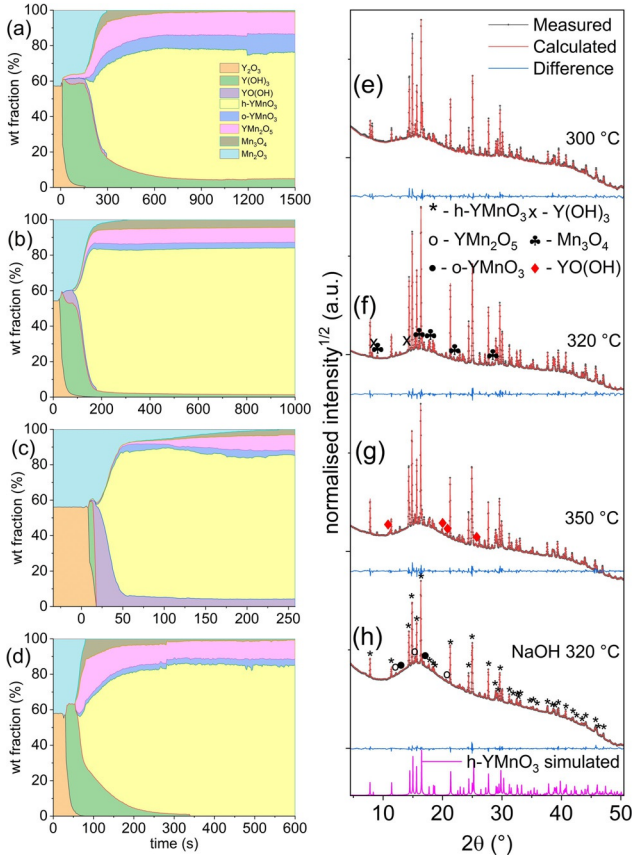


**Figure 1.** Stacked area plots of the weight fractions of observed phases over time for the reaction between $Y_2O_3$ and $Mn_2O_3$ in 5 M KOH at (a) 300 °C, (b) 320 °C, and (c) 350 °C, and (d) in 5 M NaOH at 320 °C. Integrated XRD patterns ($\lambda = 0.77445$ Å) and patterns calculated using Rietveld refinement of the final dataset for the reaction at (e) 300 °C, (f) 320 °C, and (g) 350 °C, and (h) 320 °C in 5 M NaOH.

porting Information. The reactions show different progressions; the reactions at 300 and 320 °C progresses via an intermediate stage in which the $Y_2O_3$ converts mostly to $Y(OH)_3$, and a small amount of YO(OH) which appears several seconds later before both are converted into h-$YMnO_3$ In addition, o-$YMnO_3$ and $YMn_2O_5$ are present, although some $Y(OH)_3$ remains. At 350 °C, the $Y(OH)_3$ is decomposed more easily and appears only briefly after the heat is applied before completely decomposing into YO(OH). The latter then reacts with $Mn_2O_3$ to form h-$YMnO_3$ and secondary phases, but also remaining in a significant quantity. This reaction progression ($Y_2O_3$ to $Y(OH)_3$ to YO(OH)) is in line with previously published work.[24,43] The secondary phase $YMn_2O_5$, in which Mn has an average oxidation state of 3.5, is the major secondary phase at all three temperatures. $YMn_2O_5$ forms due to charge disproportionation of Mn, leading to the concurrent formation of $Mn_3O_4$, in which Mn has an average oxidation state of $2\frac{2}{3}$. $YMn_2O_5$ being the most stable phase in the $MnO_x$-$YO_{1.5}$ phase diagram below 789 °C explains why this charge disproportionation occurs.[15] However, from weight fractions of crystalline phases alone, the oxidation states do not fully balance; for example, the average oxidation state of Mn in $YMn_2O_5$ and $Mn_3O_4$ with weight fractions of 8.5 and 2.8, respectively (as in the reaction at 320 °C in 5 M KOH) is 3.2. This average oxidation number may be accounted for by a significant error in refining weight fractions with such low intensity, or the presence of soluble $Mn^{II}$ or amorphous species not included in the Rietveld refinements. Another challenge with the hydrothermal synthesis of h-$YMnO_3$ is the appearance of significant amounts of o-$YMnO_3$ (except in the case of 1 M KOH at 320 °C). The final weight fractions of all observed phases of reactions at 300, 320 and 350 °C are shown in Table S1, where it can be seen that the reaction at 320 °C had a slightly higher proportion of h-$YMnO_3$. Using 5 M NaOH mineraliser at 320 °C, no YO(OH) was observed (Figure 1(d)). Weight fraction evolutions for experiments using 1 and 10 M KOH, as well as with a partial substitution of $Mn_2O_3$ with $Mn_3O_4$ (weight fraction) presented in Figure S2 show that the reaction performed in 1 M KOH yields very low purity, while higher KOH concentrations lead to faster reactions. Both 10 M KOH and 1 M KOH reactions led to complete dehydration of $Y(OH)_3$, and the use of $Mn_3O_4$ in the reaction resulted in a lower weight fraction of $YMn_2O_5$, although $Mn_3O_4$ remains after the reaction.

The h-$YMnO_3$ was fitted using the Stephens model for anisotropic peak broadening.[44] The evolution of the (400) and (004) Stephens parameters over time from the onset of h-$YMnO_3$ formation are shown in Figure S3. A higher Stephens parameter indicates broader peaks from planes perpendicular to the indicated crystal axis for example, a large (400) parameter means broad (*hk*0) peaks.

The reaction of $Y_2O_3$ in 5 M KOH was followed under in situ hydrothermal conditions at temperatures in the range 100 to 350 °C. After stabilising at 100 °C, three phases were observed: unreacted $Y_2O_3$, $Y(OH)_3$, and a third, unidentified phase. This third phase was not observed at 150 °C, where only $Y(OH)_3$ and a small amount of $Y_2O_3$ appeared. In the range from 280 to 330 °C, $Y(OH)_3$ was the only observed phase, and at 340 and 350 °C, YO(OH) appeared alongside $Y(OH)_3$ (Figure 2, selected XRD patterns shown in Figure S4). After cooling to room temperature, the composition did not change from this.

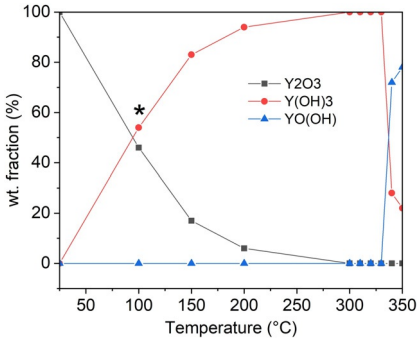


**Figure 2.** The evolution of weight fractions of different phases with increasing temperature as $Y_2O_3$ reacts in 5 M KOH solution. An unknown phase was also observed at 100 °C. The data shown are from diffraction patterns taken at equilibrium at each temperature. *An unidentified phase was observed at 100 °C, and this phase is not included in the calculations of the weight fractions.

## Kinetics

Using the scale factors extracted from the Rietveld refinement, information on the kinetics of h-$YMnO_3$ formation was analysed using the Johnson—Mehl—Avrami–Kolmogorov equation,[45,46] $\alpha = 1 - e^{kt^n}$, where $\alpha$ is the extent of reaction. This equation was used to extract vales for *k*, a rate constant related to radial crystal growth, and *n*, an exponent related to the dimensionality of crystal growth, and is indicative of the growth and transport mechanisms[46] (see Table 1). To choose appropriate values for the beginning of nucleation, the data were fitted such that the value for *n* was the same to 1 decimal place. An obtained value of $n \geq 2$ implies a reaction mechanism limited by nucleation and growth.[47,48] In this case, the evolution of $\alpha$ over time is characterised by an initial increase in rate, followed by an approximately constant rate, and a decrease in rate at the end of the reaction due to the depletion of reactants. Lower values of *n* indicate that diffusion or phase

**Table 1.** Values for rate constant *k*, exponent *n*, and coefficient of determination calculated, $R^2$, determined from the plots of normalised scale factors of h-$YMnO_3$ over reaction time using the Johnson–Mehl–Avrami–Kolmogorov model.

| Temperature [°C] | [KOH] [M] | $K$ [$s^{-1}$] | $n$ | $R^2$ |
|---|---|---|---|---|
| 320 | 1 | $1.8\times10^{-4}$ (1) | 1.4±0.01 | 0.974 |
| 300 | 5 | $1.1\times10^{-5}$ (1) | 2.4±0.03 | 0.732 |
| 320 | 5 | $7.9\times10^{-5}$ (8) | 2.4±0.03 | 0.979 |
| 320 (repeat) | 5 | $1.4\times10^{-4}$ (2) | 2.4±0.04 | 0.976 |
| 350 | 5 | $8.1\times10^{-4}$ (6) | 2.4±0.03 | 0.998 |
| 300 | 10 | $3.7\times10^{-5}$ (4) | 2.4±0.03 | 0.989 |
| 320 | 10 | $4.2\times10^{-4}$ (7) | 2.4±0.06 | 0.987 |
| 350 | 10 | $3.9\times10^{-3}$ (7) | 2.4±0.09 | 0.981 |
| 320 | 5, NaOH | $9.6\times10^{-4}$ (21) | 2.4±0.1 | 0.634 |

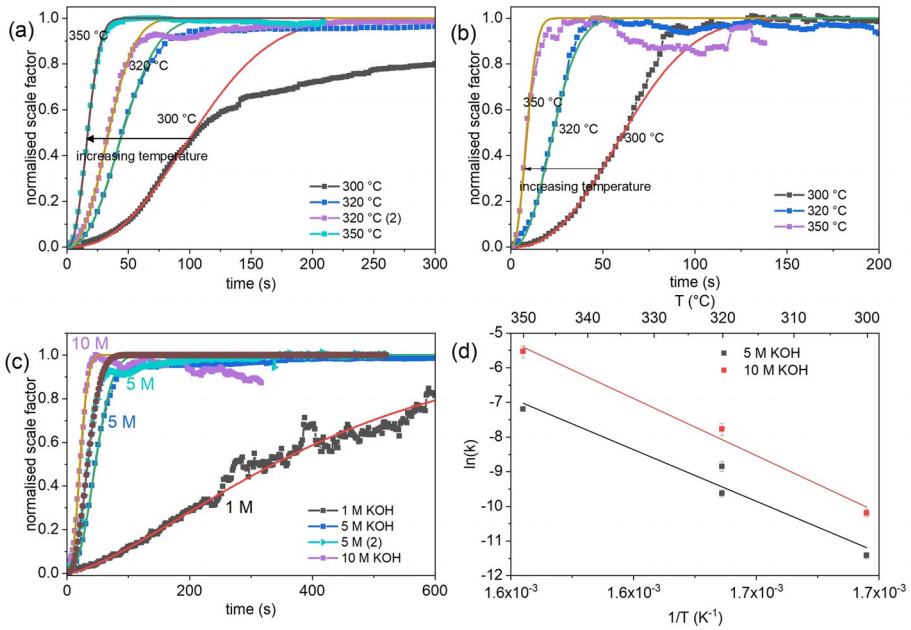


**Figure 3.** h-$YMnO_3$ scale factors and Avrami fits over time for reactions at 300, 320 and 350 °C in (a) 5 M KOH and (b) 10 M KOH, (c) evolution of h-$YMnO_3$ scale factors for reactions at 320 °C in 1, 5 and 10 M KOH, refined scale factors shown by line and scatter plots and fitted curves shown by solid lines, and (d) plot of ln(*k*) against 1/*T* for the corresponding reactions with linear regressions.

boundary growth can be limiting factors. There is one reaction where $n < 2$; the reaction with 1 M KOH at 320 °C. There appears to be a relatively linear evolution (with respect to higher KOH concentrations) of the scale factor over time. Therefore, a precursor dissolution limiting mechanism could be possible in this reaction due to the low mineraliser concentration.

Figures 3 (a) and (b) show the evolution of scale factors over time for reactions at different temperatures at 5 and 10 M KOH, respectively. At 300 °C and 5 M KOH (Figures 1 (a) and 2 (a)) and at 320 °C in 5 M NaOH (Figures 1 (g) and S4), there is an abrupt reduction in the rate of h-$YMnO_3$ formation coinciding with the exhaustion of the $Mn_2O_3$. After this there is a small reduction in the weight fractions of $Y(OH)_3$, $Mn_3O_4$ and $YMn_2O_5$ as h-$YMnO_3$ continues to form. This change in mechanism is the likely cause of the reduction in rate. Additionally, the four datasets at 320 °C and different KOH concentrations (with two reactions at 5 M) (Figure 3 (c)) show significantly different reaction rates, with higher KOH concentration increasing the reaction rate.

The progression of the quantity of h-$YMnO_3$ in reactions in 5 M KOH follows a definite trend according to the Arrhenius equation, with the linear regression giving an activation energy of $240 \pm 40$ kJ mol$^{-1}$. At 10 M KOH, a similar trend is observed with an activation energy of $270 \pm 30$ kJ mol$^{-1}$, but yielding higher *k* values for a given temperature (Figure 3 (d)). For comparison, hydrothermal processes which take place below 200 °C typically have activation energies below 100 kJ mol$^{-1}$.[49–51] The high stability of the intermediate phases (Figure 2) helps to explain the high temperature required and high activation energy for the reaction forming h-$YMnO_3$.

## Ex situ studies on autoclave synthesis

Reactions between $Y_2O_3$ and $Mn_2O_3$ to form h-$YMnO_3$ were also performed ex situ in an autoclave at 320 °C in KOH solution. Using a stoichiometric ratio of Y:Mn, a 90% phase purity was achieved (measured by Rietveld refinement) after washing the product with acid to remove $Y(OH)_3$. Using a 10% excess of $Y_2O_3$, the phase purity was improved to 98%, with minor secondary phases of $YMn_2O_5$ and $Mn_3O_4$ being observed. The XRD patterns show a large degree of preferred orientation in the (00*l*) direction, which is clearly indentifed from a simple comparison of the measured diffraction pattern and a simulated pattern of h-$YMnO_3$ without any orientation (Figure S6). The degree of orientation has been quantified by the March–Dollase model in diffraction pattern refinements (Table S2).

SEM images of the h-$YMnO_3$ formed both in situ and ex situ in the large autoclave showed similar large, flat hexagonal particles of the order of 10 μm across (Figure 4). This plate-like structure explains the preferred orientation in the XRD patterns as the plates align during sample preparation.

## Discussion

The data presented here show the progression of the reaction between the two solid precursors $Y_2O_3$ and $Mn_2O_3$. The reaction proceeds via $Y(OH)_3$ and/or YO(OH), while $Mn_2O_3$ disappears as the product appears, as shown by the weight fraction area plots in Figures 1 (a)–(d). The h-$YMnO_3$ appears concurrently with the reduction in scale factor of $Mn_2O_3$, $Y(OH)_3$, and YO(OH). It is therefore likely that any soluble species would be extremely short lived, and that heterogeneous nucleation occurs on the surfaces of intermediate phases ($Y(OH)_3$, YO(OH)

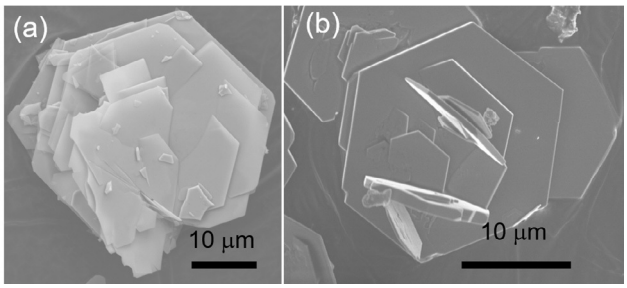


**Figure 4.** SEM images of h-$YMnO_3$ synthesised by a hydrothermal route, both (a) ex situ and (b) from the in situ capillary set-up.

or $Mn_2O_3$). It is also likely that a dissolution-precipitation mechanism occurs rather than a shrinking-core mechanism due to the fact that the $YMnO_3$ forms in distinct hexagonal shapes which do not resemble the precursors. Stampler et al. suggested from ex situ studies that the reaction requires the breakdown of $Ln(OH)_3$ into the more reactive LnO(OH) before proceeding to form h-$LnMnO_3$, while $Mn_2O_3$ is reactive at least as low as 150 °C. This was inferred from the fact that the required temperature for the reaction to proceed is heavily dependent on the stability of $Ln(OH)_3$. The ionic radius dependence of $Ln(OH)_3$ stability was reported by Klevtsov and Sheina.[43] Stampler et al. then suggested that the LnO(OH) reacts with $Mn(OH)_4^-$ to form h-$YMnO_3$. Chouaib et al.[52] and Kozawa et al.[53] showed that $Mn_2O_3$ has a solubility of ≈2 mM in 5 M KOH solution at 25 °C. This may appear to be corroborated by our results which show the formation of YO(OH) in quantities dependent on reaction temperature before the appearance of h-$YMnO_3$ (Figure 1 (a)–(c)). However, this does not conclusively prove that h-$YMnO_3$ cannot crystallise directly from $Y(OH)_3$ and $Mn_2O_3$, and in the reaction with 5 M NaOH at 320 °C, we do not observe any YO(OH) (Figure 1 (d)). A suggested mechanism for the formation of $YMnO_3$ is depicted in Figure 5. For the aforementioned reasons, we consider it likely that nucleation occurs on the surface of one of the solid precursors. We also consider it likely that Mn-species will have a higher solubility than Y-species under the reaction conditions, assuming that Y will dissolve as a positive species, the equilibrium would shift towards solid YO(OH) or $Y(OH)_3$ under a high $OH^-$ concentration.

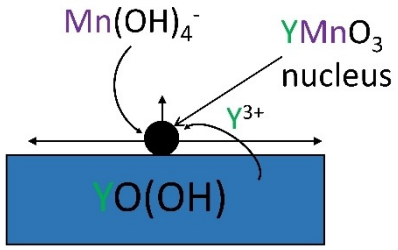


**Figure 5.** Schematic depicting the suggested mechanism of crystal growth of $YMnO_3$ under hydrothermal synthesis.

The data also show that the KOH concentration is an important factor for the reaction progression and rates. At higher KOH concentrations, the $Y(OH)_3$ dehydrates into YO(OH) much faster; even at the low temperature of 300 °C in 10 M KOH, all of the $Y(OH)_3$ eventually dehydrates (Figure S2 (b)). Related to this, we have also observed that when $Y_2O_3$ is heated in 5 M KOH solution, no dehydration of $Y(OH)_3$ occurs until 340 °C. Taken together, this implies that soluble Mn is involved catalysing the dehydration of $Y(OH)_3$, which we observe to take place at 300 °C in the presence of $Mn_2O_3$. It is also observed that using 1 M KOH leads to the concurrent formation of YO(OH) and $Y(OH)_3$, before the $Y(OH)_3$ fully dehydrates (Figure S2 (a)), which must result from a different mechanism than the observed fast dehydration at 10 M KOH.

The analysis of evolution in Stephens parameters (Figure S3) shows a trend of increasing (400) parameter and decreasing (004) parameter for all reactions. This indicates a broadening of peaks in the (*hk*0) family and a narrowing of peaks in the (00*l*) family. This means that there is an increasing crystal size anisotropy over time. Comparing the absolute values of (400) with (004) parameters is challenging however as the scales are very different. Interestingly, there appears to be little difference in final values of the (400) parameters between h-$YMnO_3$ formed in KOH under different temperature and concentration, however, in NaOH, the (400) parameter appears to be much larger; 670 for 5 M KOH at 320 °C, and 1460 for 5 M NaOH at 320 °C for the final frames. Whereas for the (004) parameter, high temperature and mineraliser concentration yielded lower values (<10 for 10 M KOH, 320 °C and 5 M KOH, 350 °C and ≈20 for reactions at 300, and 320 °C in 5 M KOH, and 320 °C in 5 M NaOH).

By comparison, many other oxide ferroelectrics, such as $BaTiO_3$,[37,38,54] $K_{1-x}Na_xNbO_3$,[39,40,55] $Sr_{1-x}Ba_xNb_2O_6$,[42] and $BiFeO_3$[41] the syntheses of which have been previously studied using in situ XRD, do not form via such stable intermediate phases, and as such can be prepared at significantly lower temperatures. These in situ studies show that the outcome and progression of a reaction is highly dependent on the specific system. For example, while $BaTiO_3$, $Sr_{1-x}Ba_xNb_2O_6$ and $KNbO_3$ appear without solid intermediate phases, $Sr_{1-x}Ba_xNb_2O_6$[42] and $KNbO_3$[55] don't appear until after several minutes suggesting the existence of soluble intermediates in the reaction. The reaction producing $NaNbO_3$ on the other hand proceeds via several shortly-lived crystalline intermediates.[55] Similarly, multiferroic $BiFeO_3$ synthesised from nitrates was observed to form highly crystalline $Bi_2O_3$, which remained stable for several minutes before $BiFeO_3$ began to crystallise, during this period the $Fe(NO_3)_3$ remained solubilised.[41]

There are still challenges to be addressed with respect to hydrothermal synthesis of h-$YMnO_3$, most notably the difficulty in synthesising phase pure h-$YMnO_3$. This is a result of the complexity of the system, with a total of eight crystalline phases having been detected throughout the course of the reaction. We suggest three possible optimization possibilities for reducing the formation of secondary phases during hydrothermal synthesis; 1) improved mixing of the precursor materials to reduce the diffusion distance between reactive species, thereby reducing the time to form secondary phases, and the use of nanoparticle precursors to increase solubility and reduce

solid state diffusion distances, 2) adding $Mn^{II}$ salt to the reaction and performing the reaction under yttrium rich conditions (then dissolving the yttrium hydroxide secondary phase in dilute acid) to reduce the propensity for $YMn_2O_5$ formation or to facilitate its reduction to h-$YMnO_3$ if it does form, and 3) using a lower pressure to reduce the o-$YMnO_3$ formation. Performing the reaction under supercritical conditions ($>374\,^{\circ}C$, $>221$ bar) may also provide a route to improving the phase purity, as Nørby et al. showed with yttrium aluminium garnet.[56]

The synthesis procedure used here can be extended to other $LnMnO_3$ materials as they are able to be synthesised under similar conditions.[24] The stability of $Ln(OH)_3$ is dependent on the Ln radius, with smaller radii yielding lower stability due to steric effects (Ln is 9-coordinated in $Ln(OH)_3$ and 7-coordinated in LnO(OH)) and increased acidity of the smaller Ln ions,[24,43,57] and so a larger range of temperatures are available for studying other systems.

Still, hydrothermal synthesis offers a fast, low-temperature method for producing h-$YMnO_3$ particles in a range of sizes and shapes which is useful for, for example, catalytic applications, with all reactions reported here taking less than 1 hour. By contrast solid-state methods for producing powder samples, are only able to produce small ($\approx$100 nm) roughly spherical particles and require much higher temperatures. Thin films are typically required for electronic device application, and the hydrothermal method has been shown to be amenable to deposition on a substrate to make polycrystalline thin films,[58,59] which could make use of the ferroic properties of h-$YMnO_3$.

## Conclusions

In conclusion, we have studied the hydrothermal synthesis of h-$YMnO_3$ from $Y_2O_3$ and $Mn_2O_3$ as precursors with hydroxide mineraliser, probed through in situ XRD for the first time. The reaction is shown to go via an intermediate period where $Y_2O_3$ is rapidly converted to $Y(OH)_3$, which is then dehydrated into YO(OH) before reacting with $Mn_2O_3$ to form h-$YMnO_3$. It is not clear whether dehydration of $Y(OH)_3$ is necessary for the reaction to occur; in the reaction performed in NaOH no YO(OH) is observed which suggests that it is not necessary. From extracted kinetic data as a function of temperature, activation energies for the reaction were estimated to be $240\pm40$ and $270\pm30$ kJ mol$^{-1}$ for the reaction in 5 and 10 M KOH, respectively, in line with the high-temperature required for the reaction to proceed due to the high stability of $Y(OH)_3$.

## Experimental Section

$Y_2O_3$ (99.9%, Alfa Aesar), $Mn_2O_3$ (99.9%, Sigma Aldrich), KOH (90%, Sigma Aldrich), NaOH (97%, Sigma Aldrich) were used for the syntheses.

In situ XRD experiments were conducted at BM01, Swiss Norwegian beamlines (SNBL) at the European Synchrotron Radiation Facility (ESRF). The temperature inside the capillary was calibrated using a hexagonal boron nitride standard prior to experiments. The wavelength of the monochromatic incident beam was 0.77445 Å, refined on a NIST-660a $LaB_6$ reference. The diffracted beam was detected using a 2D Pilatus 2M detector with acquisition times of 2 or 5 s, and processed to 1D diffraction patterns using software available on the PILATUS@SNBL platform.[60]

Samples were prepared for the in situ capillary cell[40] by weighing out $Mn_2O_3$ and $Y_2O_3$ in equal molar ratio into plastic vials, to which 2 or 5 mL KOH or NaOH solution at 1, 5 or 10 M was added, such that the concentration of Mn ions was 0.347 M. A mass ratio of 85.4:14.6 $Mn_2O_3$:$Mn_3O_4$ was used for the reaction in which $Mn_2O_3$ was partly substituted for $Mn_3O_4$, giving a 95:5 molar ratio of $Mn^{III}$:$Mn^{II}$. The reaction of $Y_2O_3$ with KOH used 0.347 M of Y ions with 5 M KOH.

Reaction mixtures were loaded into an open cell using a syringe, the cell was then sealed with a Swagelok cap screwed on at the end. For a reaction, the cell was pressurised using a Shimadzu LC-10ADvp HPLC pump to a pressure of 200 bar. This was then heated using a pre-set hot-air blower which was moved into place with a motor. The in situ cell made use of a sapphire capillary which is resistant to strongly basic conditions such as those used in this and our previous studies. Stainless-steel Swagelok parts and tubing were used to form connections between the HPLC pump and the capillary and to seal the reaction cell.[40]

High-temperature ($>250\,^{\circ}C$) ex situ reactions were conducted in a 100 mL Monel (copper-nickel alloy) autoclave. h-$YMnO_3$ was synthesised using a method similar to that described by Stampler et al.[24] $Y_2O_3$ and $Mn_2O_3$ (total 3 g) were added to the autoclave, to this, 30 mL of 5 M KOH was added, stirred for 30 min, and then heated to $320\,^{\circ}C$. It took approximately 40 min to reach the set temperature, the pressure at the set temperature was 90 and 92 bar in the stoichiometric and non-stoichiometric experiments, respectively. The total reaction time was 6 h (including time to reach the set temperature), after which the autoclave vessel slowly cooled to room temperature over a few hours. The product was collected by vacuum filtration, washed with $\approx$200 mL of deionised water and dried at $70\,^{\circ}C$ for 3 h.

All Rietveld refinements were performed using Topas 5.[61] Batch refinements of synchrotron in situ experiments were run using Topas from launch mode using JEdit with macros for interaction with Topas,[62] via a custom script written using Jupyter Notebooks[63] by our group.[55] Instrumental parameters were determined using a $LaB_6$ standard, from which the peak profile was fitted with a Thompson—Cox–Hastings pseudo-Voigt (TCHZ) peak type.[64] Crystallographic information files used in refinements were obtained from the Inorganic Crystal Structure Database provided from the following references: h-$YMnO_3$,[2] o-$YMnO_3$,[65] $Y(OH)_3$,[66] YO(OH),[67] $YMn_2O_5$,[68] $Mn_3O_4$,[69] $Y_2O_3$,[70] and $Mn_2O_3$.[71]

Fits for kinetic data were calculated using the SciPy module in Python.[72] Scale factors were normalised using the highest scale factor value in a dataset, or if there were large fluctuations in the value, the mean of the final values was taken.

Refinements of the diffractograms from the ex situ experiments were modelled by adjusting the scale factor and lattice parameters. This was followed by use of the March–Dollase model for preferred orientation in the 00*l* direction, then in the 110 direction.[73] The application of Stephens model for the hexagonal crystal system followed to account for anisotropic crystal size peak broadening.[44] $B_{iso}$ values were then refined, and finally atomic positions. In-house diffractograms were measured using a Bruker D8 A25 DaVinci X-ray Diffractometer with $Cu_{K\alpha}$ radiation, a LynxEye SuperSpeed detector, and a v6 variable incident slit.

## Acknowledgements

The authors would like to thank the Research Council of Norway (project number: 250403/F20) and NTNU Norwegian University of Science and Technology for providing funding for this work, the ESRF and the SNBL for providing beam-time to conduct experiments, and the staff at SNBL for assistance at the beam-time; D. Chernyshov and V. Dyadkin.

## Conflict of interest

The authors declare no conflict of interest.

**Keywords:** hydrothermal synthesis · in situ · synchrotron · $YMnO_3$

[1] S. C. Abrahams, *Acta Crystallogr. Sect. B* **2001**, *57*, 485 – 490.
[2] A. S. Gibbs, K. S. Knight, P. Lightfoot, *Phys. Rev. B* **2011**, *83*, 094111.
[3] M. Lilienblum, T. Lottermoser, S. Manz, S. M. Selbach, A. Cano, M. Fiebig, *Nat. Phys.* **2015**, *11*, 1070 – 1073.
[4] S. H. Skjærvø, Q. N. Meier, M. Feygenson, N. A. Spaldin, S. J. L. Billinge, E. S. Bozin, S. M. Selbach, *Phys. Rev. X* **2019**, *9*, 031001.
[5] B. B. Van Aken, T. T. M. Palstra, A. Filippetti, N. A. Spaldin, *Nat. Mater.* **2004**, *3*, 164 – 170.
[6] C. J. Fennie, K. M. Rabe, *Phys. Rev. B* **2005**, *72*, 100103.
[7] A. Muñoz, J. A. Alonso, M. J. Martínez-Lope, M. T. Casáis, J. L. Martínez, M. T. Fernández-Díaz, *Phys. Rev. B* **2000**, *62*, 9498 – 9510.
[8] M. Fiebig, T. Lottermoser, D. Fröhlich, A. V. Goltsev, R. V. Pisarev, *Nature* **2002**, *419*, 818 – 820.
[9] T. Kosub, M. Kopte, R. Hühne, P. Appel, B. Shields, P. Maletinsky, R. Hübner, M. O. Liedke, J. Fassbender, O. G. Schmidt, D. Makarov, *Nat. Commun.* **2017**, *8*, 13985.
[10] S. Remsen, B. Dabrowski, *Chem. Mater.* **2011**, *23*, 3818 – 3827.
[11] S. F. Wang, H. Yang, T. Xian, X. Q. Liu, *Catal. Commun.* **2011**, *12*, 625 – 628.
[12] H. L. Yakel Jr., W. C. Koehler, E. F. Bertaut, E. F. Forrat, *Acta Crystallogr.* **1963**, *16*, 957 – 962.
[13] J. S. Zhou, J. B. Goodenough, J. M. Gallardo-Amores, E. Morán, M. A. Alario-Franco, R. Caudillo, *Phys. Rev. B* **2006**, *74*, 014422.
[14] N. Jiang, S. M. Woodley, C. R. A. Catlow, X. Zhang, *J. Mater. Chem. C* **2015**, *3*, 4787 – 4793.
[15] M. Chen, B. Hallstedt, L. J. Gauckler, *J. Alloys Compd.* **2005**, *393*, 114 – 121.
[16] K. Bergum, H. Okamoto, H. Fjellvåg, T. Grande, M.-A. Einarsrud, S. M. Selbach, *Dalton Trans.* **2011**, *40*, 7583.
[17] C. Zhang, J. Su, X. Wang, F. Huang, J. Zhang, Y. Liu, L. Zhang, K. Min, Z. Wang, X. Lu, F. Yan, J. Zhu, *J. Alloys Compd.* **2011**, *509*, 7738 – 7741.
[18] H. W. Brinks, H. Fjellvåg, A. Kjekshus, *J. Solid State Chem.* **1997**, *129*, 334 – 340.
[19] N. N. Greenwood, A. Earnshaw in *Chemistry of the Elements*, Elsevier Science **1997**, pp. 1040 – 1044.
[20] C. Abughayada, B. Dabrowski, M. Avdeev, S. Kolesnik, S. Remsen, O. Chmaissem, *J. Solid State Chem.* **2014**, *217*, 127 – 135.
[21] S. H. Skjærvø, E. T. Wefring, S. K. Nesdal, N. H. Gaukås, G. H. Olsen, J. Glaum, T. Tybell, S. M. Selbach, *Nat. Commun.* **2016**, *7*, 13745.
[22] C. Li, K. C. K. Soh, P. Wu, *J. Alloys Compd.* **2004**, *372*, 40 – 48.
[23] R. D. Shannon, *Acta Crystallogr. Sect. A* **1976**, *32*, 751 – 767.
[24] E. S. Stampler, W. C. Sheets, W. Prellier, T. J. Marks, K. R. Poeppelmeier, *J. Mater. Chem.* **2009**, *19*, 4375 – 4381.
[25] M. H. Harunsani, J. Li, Y. B. Qin, H. T. Tian, J. Q. Li, H. X. Yang, R. I. Walton, *Appl. Phys. Lett.* **2015**, *107*, 062905.
[26] R. Dhinesh Kumar, R. Jayavel, *Mater. Lett.* **2013**, *113*, 210 – 213.
[27] Z. Zhou, L. Guo, F. Ye, *J. Alloys Compd.* **2013**, *571*, 123 – 131.
[28] P. Norby, A. N. Christensen, J. C. Hanson, *Stud. Surf. Sci. Catal.* **1994**, *84*, 179 – 186.
[29] P. Norby, *J. Am. Chem. Soc.* **1997**, *119*, 5215 – 5221.
[30] R. I. Walton, D. O'Hare, *Chem. Commun.* **2000**, 2283 – 2291.
[31] R. I. Walton, R. J. Francis, P. S. Halasyamani, D. O'Hare, R. I. Smith, R. Done, R. J. Humphreys, *Rev. Sci. Instrum.* **1999**, *70*, 3391 – 3396.
[32] J. S. O. Evans, R. J. Francis, D. O'Hare, S. J. Price, S. M. Clark, J. Flaherty, J. Gordon, A. Nield, C. C. Tang, *Rev. Sci. Instrum.* **1995**, *66*, 2442 – 2445.
[33] M. Bremholm, M. Felicissimo, B. B. Iversen, *Angew. Chem. Int. Ed.* **2009**, *48*, 4788 – 4791; *Angew. Chem.* **2009**, *121*, 4882 – 4885.
[34] A. R. M. Dalod, O. G. Grendal, S. L. Skjærvø, K. Inzani, S. M. Selbach, L. Henriksen, W. Van Beek, T. Grande, M. A. Einarsrud, *J. Phys. Chem. C* **2017**, *121*, 11897 – 11906.
[35] C. Tyrsted, K. M. Ornsbjerg Jensen, E. D. Bøjesen, N. Lock, M. Christensen, S. J. L. Billinge, B. B. Iversen, *Angew. Chem. Int. Ed.* **2012**, *51*, 9030 – 9033; *Angew. Chem.* **2012**, *124*, 9164 – 9167.
[36] R. I. Walton, F. Millange, R. I. Smith, T. C. Hansen, D. O'Hare, *J. Am. Chem. Soc.* **2001**, *123*, 12547 – 12555.
[37] G. Philippot, K. M. Ø. Jensen, M. Christensen, C. Elissalde, M. Maglione, B. B. Iversen, C. Aymonier, *J. Supercrit. Fluids* **2014**, *87*, 111 – 117.
[38] O. G. Grendal, A. B. Blichfeld, S. L. Skjærvø, W. van Beek, S. M. Selbach, T. Grande, M. Einarsrud, *Crystals* **2018**, *8*, 253.
[39] D. R. Modeshia, R. J. Darton, S. E. Ashbrook, R. I. Walton, *Chem. Commun.* **2009**, 68 – 70.
[40] S. L. Skjærvø, K. H. Wells, W. van Beek, T. Grande, M.-A. Einarsrud, *CrystEngComm* **2018**, *20*, 6795 – 6802.
[41] J. L. Mi, T. N. Jensen, M. Christensen, C. Tyrsted, J. E. Jørgensen, B. B. Iversen, *Chem. Mater.* **2011**, *23*, 1158 – 1165.
[42] O. G. Grendal, A. B. Blichfeld, T. D. Vu, W. van Beek, S. M. Selbach, T. Grande, M.-A. Einarsrud, *CrystEngComm* **2019**, *21*, 5922 – 5930.
[43] P. V. Klevtsov, L. P. Sheina, *Izv. Akad. Nauk SSSR, Neorg. Mater.* **1965**, *1*, 912 – 917.
[44] P. W. Stephens, *J. Appl. Crystallogr.* **1999**, *32*, 281 – 289.
[45] M. Avrami, *J. Chem. Phys.* **1939**, *7*, 1103 – 1112.
[46] K. M. Ø. Jensen, C. Tyrsted, M. Bremholm, B. B. Iversen, *ChemSusChem* **2014**, *7*, 1594 – 1611.
[47] J. D. Hancock, J. H. Sharp, *J. Am. Ceram. Soc.* **1972**, *55*, 74 – 77.
[48] J. H. Sharp, G. W. Brindley, B. N. N. Achar, *J. Am. Ceram. Soc.* **1966**, *49*, 379 – 382.
[49] B. L. Gersten in *Crystal Growth Technology* (Eds.: K. Byrappa, W. Michaeli, E. Weber, T. Ohachi, H. Warlimont), William Andrew Inc., Norwich, **2003**, pp. 312 – 318.
[50] W. Hertl, *J. Am. Ceram. Soc.* **1988**, *71*, 879 – 883.
[51] G. A. Rossetti, D. J. Watson, R. E. Newnham, J. H. Adair, *J. Cryst. Growth* **1992**, *116*, 251 – 259.
[52] F. Chouaib, P. H. Heubel, M. Del Carmen Sanson, G. Picard, B. Tremillon, *J. Electroanal. Chem.* **1981**, *127*, 179 – 193.
[53] A. Kozawa, T. Kalnoki-Kis, J. F. Yeager, *J. Electrochem. Soc.* **1966**, *113*, 405 – 409.
[54] R. I. Walton, R. I. Smith, F. Millange, I. J. Clark, D. C. Sinclair, D. O'Hare, *Chem. Commun.* **2000**, 1267 – 1268.
[55] S. L. Skjærvø, S. Sommer, P. Nørby, E. D. Bøjesen, T. Grande, B. B. Iversen, M.-A. Einarsrud, *J. Am. Ceram. Soc.* **2017**, *100*, 3835 – 3842.
[56] P. Nørby, K. M. Ø. Jensen, N. Lock, M. Christensen, B. B. Iversen, *RSC Adv.* **2013**, *3*, 15368 – 15374.
[57] S. Mroczkowski, J. Eckert, H. Meissner, J. C. Doran, N. Haven, *J. Cryst. Growth* **1970**, *7*, 333 – 342.
[58] P. M. Rørvik, Å. Almli, A. T. J. Van Helvoort, R. Holmestad, T. Tybell, T. Grande, M. A. Einarsrud, *Nanotechnology* **2008**, *19*, 225605.
[59] K. Shimomura, T. Tsurumi, Y. Ohba, M. Daimon, *Jpn. J. Appl. Phys.* **1991**, *30*, 2174 – 2177.
[60] V. Dyadkin, P. Pattison, V. Dmitriev, D. Chernyshov, *J. Synchrotron Radiat.* **2016**, *23*, 825 – 829.
[61] A. A. Coelho, *J. Appl. Crystallogr.* **2000**, *33*, 899 – 908.
[62] J. S. O. Evans, *Mater. Sci. Forum* **2010**, *651*, 1 – 9.
[63] T. Kluyver, B. Ragan-Kelley, F. Pérez, B. Granger, M. Bussonnier, J. Frederic, K. Kelley, J. Hamrick, J. Grout, S. Corlay, P. Ivanov, D. Avila, S. Abdalla, C. Willing in *Positioning and Power in Academic Publishing: Players. Agents and Agendas* (Eds.: F. Loizides, B. Schmidt), IOS Press, Amsterdam, **2016**, pp. 87 – 90.
[64] P. Thompson, D. E. Cox, J. B. Hastings, *J. Appl. Crystallogr.* **1987**, *20*, 79 – 83.
[65] M. N. Iliev, M. V. Abrashev, H.-G. Lee, V. N. Popov, Y. Y. Sun, C. Thomsen, R. L. Meng, C. W. Chu, *Phys. Rev. B* **1998**, *57*, 2872 – 2877.

 

[66] G. W. Beall, W. O. Milligan, H. A. Wolcott, *J. Inorg. Nucl. Chem.* **1977**, *39*, 65 – 70.
[67] R. F. Klevtsova, P. V. Klevtsov, *J. Struct. Chem.* **1965**, *5*, 795 – 797.
[68] G. Liu, W. Wong-Ng, J. A. Kaduk, L. P. Cook, *Phys. C* **2010**, *470*, 345 – 351.
[69] D. Jarosch, *Mineral. Petrol.* **1987**, *37*, 15 – 23.
[70] M. Faucher, J. Pannetier, *Acta Crystallogr. Sect. B* **1980**, *36*, 3209 – 3211.
[71] S. Geller, *Acta Crystallogr. Sect. B* **1971**, *27*, 821 – 828.
[72] K. J. Millman, M. Aivazis, *Comput. Sci. Eng.* **2011**, *13*, 9 – 12.
[73] W. A. Dollase, *J. Appl. Crystallogr.* **1986**, *19*, 267 – 272.

Manuscript received: January 31, 2020
Accepted manuscript online: March 4, 2020
Version of record online: May 12, 2020

 